

Tunable ultrafast electron transfer in WSe₂-graphene heterostructure enabled by atomically stacking order

Xiao Xing^{1‡}, *Zeyu Zhang*^{2‡}, *Chenjing Quan*^{1, 3}, *Litao Zhao*⁴, *Chunwei Wang*¹, *Tingyuan Jia*¹, *Junfeng Ren*⁵, *Juan Du*^{1, 2*}, *Yuxin Leng*^{1, 2*}

¹State Key Laboratory of High Field Laser Physics and CAS Center for Excellence in Ultra-intense Laser Science, Shanghai Institute of Optics and Fine Mechanics (SIOM), Chinese Academy of Sciences (CAS), Shanghai 201800, China

²Hangzhou Institute for Advanced Study and Center of Materials Science and Optoelectronics Engineering, University of Chinese Academy of Sciences, Hangzhou 310024, China

³ School of Physics Science and Engineering, Tongji University, Shanghai 200092, China

⁴Key Laboratory of Spin Electron and Nanomaterials of Anhui Higher Education Institutes, Suzhou University, Suzhou 234000, People's Republic of China

⁵ School of Physics and Electronics, Shandong Normal University, Jinan, 250014, China.

Email: dujuan@mail.siom.ac.cn and lengyuxin@mail.siom.ac.cn

1 Sample preparation

Large area monolayer graphene and WSe₂ were grown by chemical vapor deposition (CVD)^{1,2}, respectively. The typical PMMA-assisted wet transfer method was used to stack the Gr/WSe₂ and WSe₂/Gr heterostructures.³

Large-area monolayer (ML) graphene grown by CVD on copper foils¹ and transferred onto a sapphire substrate using a poly (methyl methacrylate) (PMMA)-mediated transfer method.³ Large-area ML graphene was grown on copper foils at 1000°C by a CVD method using 200 sccm argon and 20 sccm hydrogen as the growth cleaning gas, 10 sccm methane as the carbon source as reported elsewhere.¹

The continuous WSe₂ ML was direct growth on a sapphire substrate by the CVD system.² High purity WO₃ was placed in a ceramic boat at the heating center of the furnace. WO₃ was heated by heating tape (1000°C), and Se powder was heated by heating tape (250°C) and carried by Ar and H₂ (Ar=200sccm, H₂=20sccm) to the furnace heating center. A sapphire substrate was placed on the downstream side 150 mm away from the ceramic boat (about 850 °C), and the growth time was 20 minutes.

WSe₂/Gr heterostructure:

To stack the WSe₂ ML on graphene, First, Large-area ML graphene was grown on copper foils, and then transferred onto a sapphire substrate using a poly (methyl methacrylate) (PMMA)-mediated transfer method.³ After that, a layer of PMMA thin film was coated on the WSe₂/sapphire as a transfer supporting layer. After the wet etching of sapphire by KOH solution, the PMMA-supported WSe₂ film was transferred to the top of the graphene/sapphire substrate, followed by the removal of PMMA using acetone.

Gr /WSe₂ heterostructure:

To stack the graphene ML on WSe₂, a layer of PMMA thin film was coated on the graphene/Cu foil as a transfer supporting layer. After the wet etching of Cu by an aqueous solution containing Fe³⁺ ions, the PMMA-supported graphene film was transferred to the top of the as-grown WSe₂ ML film, followed by the removal of PMMA using acetone.

The schematic of the two heterostructures is shown below in Fig.S1(a)-(b).

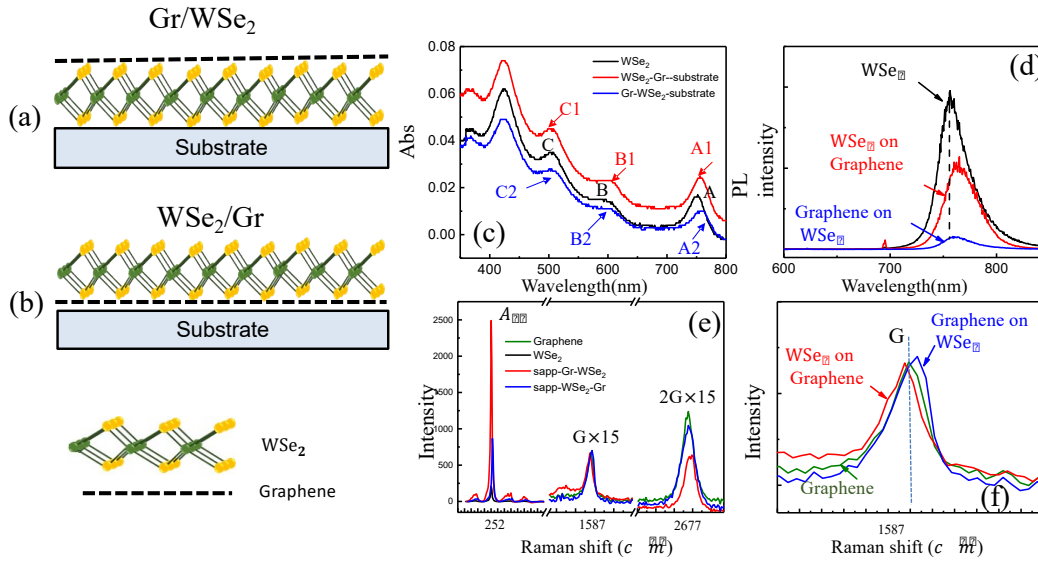


Figure. S1(a-b)) Schematic of the two heterostructures Gr/WSe₂(upper) and WSe₂/Gr (lower) (c) UV-visible absorption spectra for WSe₂ (black) , WSe₂/Gr heterostructure(red) and Gr/WSe₂ heterostructure(blue); (d) PL spectra of pristine ML WSe₂ (black), WSe₂/Gr heterostructure (red) and Gr/WSe₂ heterostructure (blue) at the room temperature. (e) The normal Raman spectra of the graphene (green), WSe₂ (black), WSe₂/Gr heterostructure (red), and Gr/WSe₂ heterostructure (blue) at the room temperature. (f) Zoom in the Raman G band of the ML graphene (green), WSe₂/Gr heterostructure (red) and Gr/WSe₂ heterostructure (blue).⁴

2 Time-resolved THz spectroscopy (TRTS)

Time-resolved THz spectroscopy was performed by using 35 fs, 1 kHz Ti: sapphire regenerative amplifier system with an 800nm central wavelength. The THz pulses were generated and detected with a pair of 1 mm thick, (110) oriented ZnTe crystals.⁵ The spot size on the sample was 0.16 cm² for the THz beam and 0.25 cm² for the pump beam. We measured the visible to mid-infrared-pump-induced modulation of the THz electric field transmission (ΔE) normalized to the THz transmission without photoexcitation (E_0) for the same sample as a function of the pump-probe delay Δt . All measurements were performed at room temperature.

3 Absorption 、 Raman and PL spectroscopy

The UV-visible absorption spectra of CVD-grown ML WSe₂ and the two stacking order vdW heterostructures are shown in Fig. S1 (c). Three prominent absorption peaks are observed

in the ML WSe₂, which are labeled as A, B, and C in the figure. The A and B peaks come from excitonic transitions between the two highest valence bands, which are split by the spin-orbit coupling, and the lowest conduction band at K and K' points of the Brillouin zone. The strong absorption in C peak at higher photon energies originates from excitonic transitions near the Λ point in the Brillouin zone, which has a high density of states.⁶ The absorption spectroscopy shows that the A-exciton binding energy in Gr/WSe₂/sapphire and WSe₂/Gr/sapphire are red-shift in contrast to the ML WSe₂.

According to the absorption spectroscopy, the bandgap can be calculated by the relation between absorption coefficient (α) and incident photon energy ($h\nu$) as: $\alpha h\nu = A(h\nu - E_g)^n$, where A is an energy independent constant; E_g is optical energy band gap of the material and the exponent n depends on the type of transition. For semiconductors, n = 1/2 values corresponding to the direct transition. Generally, the monolayer WSe₂ is direct bandgap system and hence the plot of $(\alpha h\nu)^2$ versus the photon energy ($h\nu$) (Tauc plot) is expected to show linear behavior in the higher energy region, which corresponds to a strong absorption near the absorption edge. Extrapolating the linear portion to zero absorption coefficient ($\alpha=0$) results the optical bandgap energy of the film.⁷ Here, the excitonic effects in WSe₂ are neglected. As shown in Figure S2, the bandgap of WSe₂/Gr/sapphire and Gr/WSe₂/sapphire are calculated to be 1.59eV and 1.60eV, which is smaller than the WSe₂/sapphire (1.61eV).

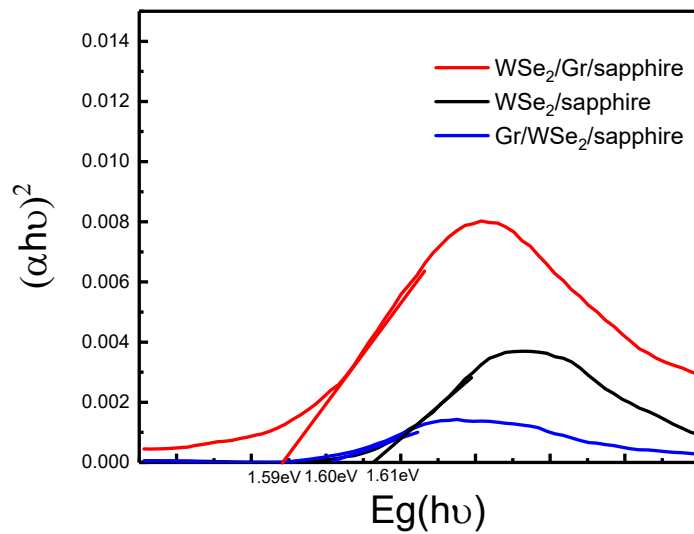


Figure. S2 the energy band calculation of the heterostructures and ML WSe₂

The photoluminescence (PL) spectra of ML WSe₂ and the two vdW heterostructures are shown in Fig. S1 (d). The PL quenching was found in the two heterostructures compared to ML WSe₂ for the interlayer coupling between the graphene and WSe₂.⁸⁻¹¹ The typical Raman spectra were taken from the two heterostructures and the individual monolayer graphene are shown in Fig. S1 (e). The featured Raman mode A_{1g} of ML WSe₂ is observed at ~252 cm⁻¹, which is consistent with the previous report.¹² Also, the absence of the B_{2g}¹ mode peaking at ~304 cm⁻¹ suggested that the flakes are MLs. The peaks centered at 1588 cm⁻¹ and 2687 cm⁻¹ are the characteristics of G and 2D bands for ML graphene.¹³ Fig.S1 (f) presents the amplified G band spectra in Fig. S1 (c). In contrast to the G band of ML graphene (peak at 1588 cm⁻¹), the G band of WSe₂/ Gr heterostructure was blue-shifted by ~1 cm⁻¹, but was red-shifted by ~2 cm⁻¹ in Gr/WSe₂ heterostructure, indicating that the charge-transfer between WSe₂ and graphene was different in the two heterostructures.

4. The contrast dynamics of photoinduced THz conductivities ($\Delta\sigma$) of the two stacks heterostructures between the photo energy of 1.55eV and 3.1 eV

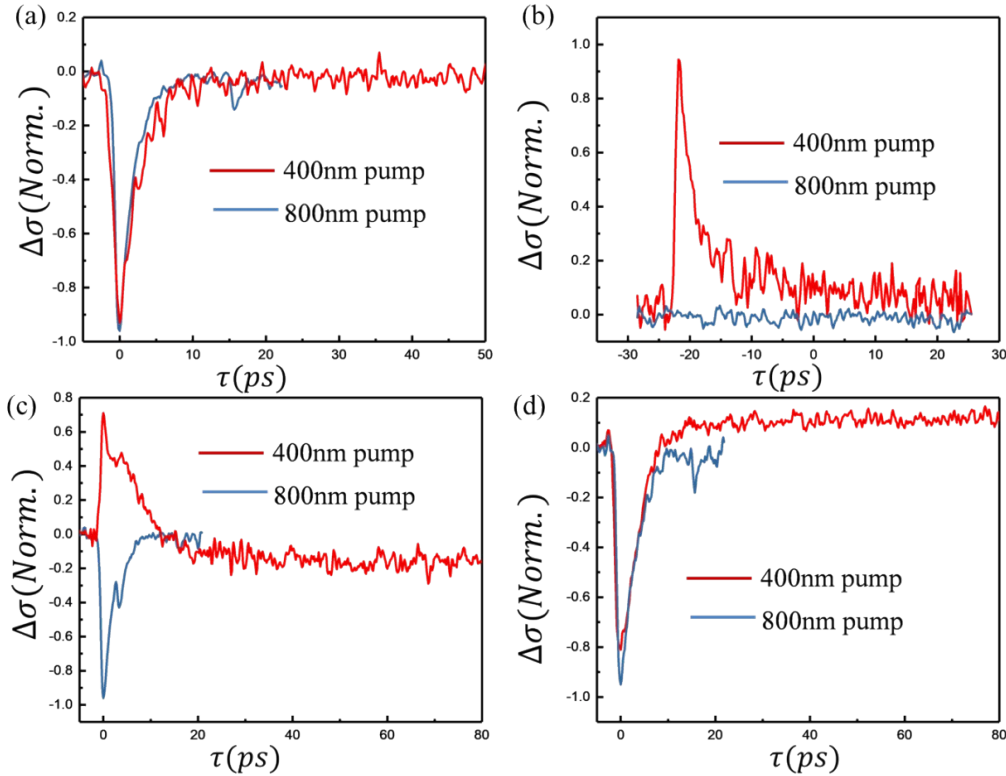


Figure. S3(a)-(d) The contrast of photoinduced terahertz conductivity ($\Delta\sigma$) between the pump energy 3.1 eV (400nm pump) and 1.55 eV (800nm pump) in graphene (a) , monolayer WSe₂ (b), the WSe₂/Gr heterostructure(c) and Gr/WSe₂ heterostructure(d) , with the pump fluence 30 $\mu\text{J}/\text{cm}^2$.

Fig. S3(a)-(d) show the normalized photoinduced THz conductivities ($\Delta\sigma$) of the two stacks heterostructures and its constituent monolayers as a function of optical pump-THz probe delay, with the photon energy of 1.55 eV and an optical pump fluence fixed at 30 $\mu\text{J}/\text{cm}^2$. The THz signal of the two heterostructures both display the THz signal of graphene with the pump energy of 1.55 eV (as shown in the blue lines). For monolayer graphene, the THz signal of both the 400nm pump and 800 nm pump is the same. Fig.S3 (b) shows that the 800nm pump can not excite the electron-hole pairs in the WSe₂ monolayer. For the heterostructures, the WSe₂ is used as light absorption material. For WSe₂/Gr/sapphire, when the sample is excited by 400 nm, the photoexcited electron-hole pairs in WSe₂ can be transferred through the two layers according to the built-in electric field. However, when the sample is excited by 800nm, the carriers transferred are less, so that it displays the THz signal of graphene. The same explanation for the Gr/WSe₂/sapphire.

5. The photoconductivity of WSe₂ monolayer with the photon energy of 1.65 eV

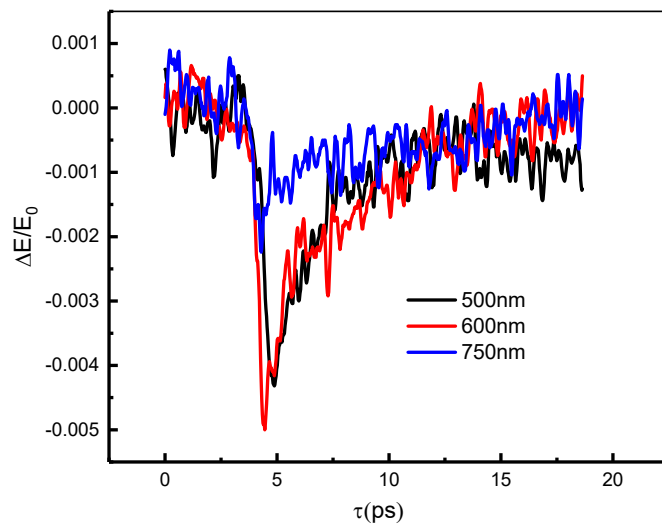


Figure. S4 TRTS carrier dynamics for WSe₂ with the photon energy above A-exciton.

6. The relationship between the photoinduced terahertz conductivity in the heterostructures and the variation of photoinduced terahertz electric field

a) The photoinduced terahertz conductivity($\Delta\sigma_{CT}$) which reflected the numbers of charge transfer electrons between the individual layers in the heterostructure, can be calculated as :

$$\Delta\sigma_{CT} = \Sigma - \Delta\sigma_0 \quad (S1)$$

$$\Delta\sigma_0 = - \frac{n+1}{Z_0} \frac{\Delta E}{E_0} \quad (S2)$$

$$\Delta\sigma_{CT} = \Sigma + \frac{n+1}{Z_0} \frac{\Delta E}{E_0} \quad (S3)$$

Where Σ is the photoinduced terahertz conductivity of monolayer graphene, $\Delta\sigma_{CT}$ is the variation of photoinduced terahertz conductivity induced by the charge transfer process. $\Delta\sigma_0$ is photoinduced terahertz conductivity of the heterostructure. ΔE_h is the variation of photoinduced terahertz electric field for heterostructure.

- 1) when Σ is a fixed constant, from the equation (S3), we noted that $\Delta\sigma_{CT} \propto \frac{\Delta E}{E_0}$.
- 2) when Σ is not a fixed constant, from the equation (S3),

$$\Delta\sigma_{CT} = \Sigma + \frac{n+1}{Z_0} \frac{\Delta E}{E_0} = - \frac{n+1}{Z_0} \left(\frac{\Delta E_g}{E_0} - \frac{\Delta E}{E_0} \right) = - \frac{n+1}{Z_0} [\Delta(\Delta E/E_0)], \quad (S4)$$

Where ΔE_g is a variation of photoinduced terahertz electric field for monolayer graphene, thus we noted that $|\Delta\sigma_{CT}| \propto [\Delta(\Delta E/E_0)]$.

7. The superlinear-to-sublinear pump-fluence dependence of CT dynamics

We attributed this superlinear-to-sublinear pump fluence dependence of CT dynamics to a transition between two distinct CT regimes: hot-electron transfer via photo-thermionic emission for sub-A-exciton excitation and direct electron (or hole) transfer for above-A-exciton excitation.

The superlinear feature is considered to be that: with increasing fluence, the electron

temperature increases, which can result in an increased CT efficiency at high fluence.

The sublinear feature can be understood as follows: with increasing fluence, many-body effects, for instance, exciton-exciton annihilation in TMDCs¹⁴, or Auger recombination in graphene, can play a critical role in the carrier dynamics on the subpicosecond to picosecond time scale. These many-body effects can result in a decrease in the electron density or hole density, which reduces the CT efficiency at high fluence.¹⁵

8. The relative CT efficiency in Gr/WSe₂ and WSe₂/Gr heterostructure

$$\alpha_{abs} = 1 - 10^{-A} \quad (S5)$$

$$N_{abs} = \frac{E \alpha}{Ah\nu} \quad (S6)$$

$$N_{CT}(h\nu) \propto \Delta[(\Delta E/E)_{max}] \quad (S7)$$

Where α_{abs} is the absorption coefficient. The relative CT efficiency is calculated through the Formulars above.

9. The connection between the semiconductor band-gap/band-edges estimation/A-exciton binding energy estimation and the CT efficiency contrast

The bandgap and the exciton properties can be influenced by the layer thickness, dielectric environment and the coulomb engineering.¹⁶⁻¹⁸Hence, the connection between the semiconductor band-gap/band-edges estimation/A-exciton binding energy estimation and the CT efficiency contrast should be discussed.

As the bandgap of the encapsulated WSe₂ has been calculated: the bandgap of WSe₂/Gr/sapphire and Gr/WSe₂/sapphire are calculated to be 1.59eV and 1.60eV, which is smaller than the WSe₂/sapphire (1.61eV). The CT rate should increase with the greater bandgap variation in the heterostructure. The bandgap variation of WSe₂/Gr/sapphire is greater than that of Gr/WSe₂/sapphire, Hence, WSe₂/Gr/sapphire should display the greater CT rate. However, this is not consistent with our results: For sub-A-exciton excitation, Gr/WSe₂/sapphire exhibit a higher CT efficiency than WSe₂/Gr heterostructure.

Therefore, we concluded that the semiconductor band-gap/band-edges estimation/A-exciton binding energy estimation was not the dominant parameter to influence the charge transfer process.

Reference:

1. X. Li, W. Cai, J. An, S. Kim, J. Nah, D. Yang, R. Piner, A. Velamakanni, I. Jung, E. Tutuc, S. K. Banerjee, L. Colombo and R. S. Ruoff, *Science*, 2009, **324**, 1312.
2. B. Liu, M. Fathi, L. Chen, A. Abbas, Y. Ma and C. Zhou, *ACS Nano*, 2015, **9**, 6119-6127.
3. A. Reina, X. Jia, J. Ho, D. Nezich, H. Son, V. Bulovic, M. S. Dresselhaus and J. Kong, *Nano Letters*, 2009, **9**, 30-35.
4. X. Xing, L. Zhao, W. Zhang, Z. Wang, H. Su, H. Chen, G. Ma, J. Dai and W. Zhang, *Nanoscale*, 2020, **12**, 2498-2506.
5. X. Xing, L. Zhao, Z. Zhang, X. Liu, K. Zhang, Y. Yu, X. Lin, H. Y. Chen, J. Q. Chen, Z. Jin, J. Xu and G.-h. Ma, *The Journal of Physical Chemistry C*, 2017, **121**, 20451-20457.
6. K. Wang, B. Huang, M. Tian, F. Ceballos, M.-W. Lin, M. Mahjouri-Samani, A. Boulesbaa, A. A. Puzos, C. M. Rouleau, M. Yoon, H. Zhao, K. Xiao, G. Duscher and D. B. Geohegan, *ACS Nano*, 2016, **10**, 6612-6622.
7. K. S. Usha, R. Sivakumar and C. Sanjeeviraja, *Journal of Applied Physics*, 2013, **114**, 123501.
8. B. Yang, E. Molina, J. Kim, D. Barroso, M. Lohmann, Y. Liu, Y. Xu, R. Wu, L. Bartels, K. Watanabe, T. Taniguchi and J. Shi, *Nano Letters*, 2018, **18**, 3580-3585.
9. G. W. Shim, K. Yoo, S.-B. Seo, J. Shin, D. Y. Jung, I.-S. Kang, C. W. Ahn, B. J. Cho and S.-Y. Choi, *ACS Nano*, 2014, **8**, 6655-6662.
10. A. Azizi, S. Eichfeld, G. Geschwind, K. Zhang, B. Jiang, D. Mukherjee, L. Hossain, A. F. Piasecki, B. Kabius, J. A. Robinson and N. Alem, *ACS Nano*, 2015, **9**, 4882-4890.
11. Y.-C. Lin, C.-Y. S. Chang, R. K. Ghosh, J. Li, H. Zhu, R. Addou, B. Diaconescu, T. Ohta, X. Peng, N. Lu, M. J. Kim, J. T. Robinson, R. M. Wallace, T. S. Mayer, S. Datta, L.-J. Li and J. A. Robinson, *Nano Letters*, 2014, **14**, 6936-6941.
12. H. Sahin, S. Tongay, S. Horzum, W. Fan, J. Zhou, J. Li, J. Wu and F. M. Peeters, *Physical Review B*, 2013, **87**, 165409.
13. A.-Y. Lu, S.-Y. Wei, C.-Y. Wu, Y. Hernandez, T.-Y. Chen, T.-H. Liu, C.-W. Pao, F.-R. Chen, L.-J. Li and Z.-Y. Juang, *RSC Advances*, 2012, **2**, 3008-3013.
14. D. Sun, Y. Rao, G. A. Reider, G. Chen, Y. You, L. Brézin, A. R. Harutyunyan and T. F. Heinz, *Nano Letters*, 2014, **14**, 5625-5629.
15. S. Fu, I. du Fossé, X. Jia, J. Xu, X. Yu, H. Zhang, W. Zheng, S. Krasel, Z. Chen, Z. M. Wang, K.-J. Tielrooij, M. Bonn, A. J. Houtepen and H. I. Wang, *Science Advances*, 2021, **7**, eabd9061.
16. L. Meckbach, T. Stroucken and S. W. Koch, *Physical Review B*, 2018, **97**, 035425.
17. L. M. Schneider, S. Lippert, J. Kuhnert, O. Ajayi, D. Renaud, S. Firoozabadi, Q. Ngo, R. Guo, Y. D. Kim, W. Heimbrod, J. C. Hone and A. Rahimi-Iman, *Nano-Structures & Nano-Objects*, 2018, **15**, 84-97.
18. A. Raja, A. Chaves, J. Yu, G. Arefe, H. M. Hill, A. F. Rigosi, T. C. Berkelbach, P. Nagler, C. Schüller, T. Korn, C. Nuckolls, J. Hone, L. E. Brus, T. F. Heinz, D. R. Reichman and A. Chernikov, *Nature Communications*, 2017, **8**, 15251.

